

Yttrium-substituted nanocrystalline TiO₂ photoanodes for perovskite based heterojunction solar cells†

Cite this: *Nanoscale*, 2014, 6, 1508

Peng Qin,^a Anna L. Domanski,^b Aravind Kumar Chandiran,^a Rüdiger Berger,^b Hans-Jürgen Butt,^b M. Ibrahim Dar,^a Thomas Moehl,^a Nicolas Tetreault,^a Peng Gao,^a Shahzada Ahmad,^{*c} Mohammad K. Nazeeruddin^{*a} and Michael Grätzel^{*a}

We report the use of Y³⁺-substituted TiO₂ (0.5%Y–TiO₂) in solid-state mesoscopic solar cells, consisting of CH₃NH₃PbI₃ as the light harvester and spiro-OMeTAD as the hole transport material. A power conversion efficiency of 11.2% under simulated AM 1.5 full sun illumination was measured. A 15% improvement in the short-circuit current density was obtained compared with pure TiO₂, due to the effect of Y³⁺ on the dimensions of perovskite nanoparticles formed on the semiconductor surface, showing that the surface modification of the semiconductor is an effective way to improve the light harvesters' morphology and electron transfer properties in the solid-state mesoscopic solar cells.

Received 5th November 2013
Accepted 5th November 2013

DOI: 10.1039/c3nr05884k

www.rsc.org/nanoscale

The conversion of solar energy to electrical current using thin film third generation photovoltaics (PV) is being widely explored for the last two decades. Sandwich/monolithic-type PV devices, consisting of a mesoporous photoanode with an organic/inorganic light harvester, a redox electrolyte/solid-state hole conductor, and a counter electrode, have attracted significant interest due to the ease of fabrication, flexibility in the selection of materials and cost-effective production.^{1,2} Recently, organometallic halide perovskite based on tin (CsSnX₃)³ or lead (CH₃NH₃PbX₃)^{4–7} has been introduced to replace traditional metal–organic complexes or organic molecules as the light harvester. The lead perovskite shows a power conversion efficiency (PCE) of 6.54% in liquid electrolyte-based devices⁸ and >15% in solid-state devices.^{9,10}

The optimal protocol for the deposition of CH₃NH₃PbX₃ on TiO₂ is achieved by spin-coating the precursor (CH₃NH₃X and PbX₂, X = Cl, Br, I) solution on the mesoporous TiO₂ film, followed by a low temperature annealing step. The annealing process results in crystalline CH₃NH₃PbX₃.^{4,7,9} The interface between TiO₂ and CH₃NH₃PbX₃ is a crucial factor in

determining crystal growth of the absorber and charge separation. The interfacial treatment and the bulk modification of TiO₂ to alter the electronic structure have shown, in many instances, the enhancement of charge injection and collection and, at the same time, the reduction of the carrier recombination.^{11–16} In the past, in an inorganic CuInS₂-sensitized TiO₂ mesoscopic solar cell, the interfacial treatment with indium sulfide was shown to reduce interface defects and to improve the PCE of the device.¹⁷ In order to modify the electronic structure of TiO₂ by an aliovalent substitution of cations in the crystal lattice, we put forward our present strategy. Earlier in the liquid-based mesoscopic cells, we have shown that the substitution with Nb⁵⁺, Ga³⁺ and Y³⁺ can significantly affect the electron transfer properties.^{11,12} Among them, Y³⁺ worked as a lead performer due to its ability in blocking the electron recombination and resulted in increased charge collection efficiency. We have noted a significant variation in the dye loading ability due to the change of the surface acid-base property of TiO₂.¹²

In our current attempt, the application of 0.5%Y³⁺-substituted TiO₂ (0.5%Y–TiO₂) in the solid state heterojunction solar cells, using methylammonium lead iodide (CH₃NH₃PbI₃) as the light harvester and 2,2',7,7'-tetrakis-(*N,N*-di-*p*-methoxyphenylamine)-9,9'-spirobifluorene (spiro-OMeTAD) as the hole transport material (HTM) leads to a PCE of 11.2% under simulated AM 1.5 full sun illumination.

Results and discussion

Photoanode characterization

The TiO₂ paste preparation is shown in the ESI.† The previous work has shown that the Y was found in negligible concentration, however, the lattice parameters of the reference anatase

^aLaboratory of Photonics and Interfaces, Department of Chemistry and Chemical Engineering, Swiss Federal Institute of Technology, Station 6, CH-1015 Lausanne, Switzerland. E-mail: mdkhaja.nazeeruddin@epfl.ch; michael.graetzel@epfl.ch

^bMax Planck Institute for Polymer Research, Ackermannweg 10, 55128 Mainz, Germany

^cAbengoa Research, C/ Energía Solar nº 1, Campus Palmas Altas-41014, Sevilla, Spain. E-mail: shahzada.ahmad@research.abengoa.com

† Electronic supplementary information (ESI) available: Paste preparation; the HRTEM micrograph of dark coloured individual nanoparticles deposited on TiO₂; histogram plots of solar cell performance parameters for 15 cells based on TiO₂; the Nyquist plot of the device without Y at 500 mV forward bias. See DOI: 10.1039/c3nr05884k

TiO₂ were modified. The inclusion of Y³⁺ increased the *a* parameter from 3.7856 Å to 3.7864 Å and decreased the *c* lattice cell parameter from 9.5013 Å to 9.4977 Å. These changes, according to Vegard's law, evidence the presence of Y³⁺ in the lattice.¹²

The Brunauer–Emmett–Teller (BET) analysis shows that 0.5%Y–TiO₂ exhibits an average particle size of 19 nm, a pore size of 24 nm, with a surface area of 83 m² g⁻¹. The 0.5%Y–TiO₂ was then used as a photoanode to fabricate PV cells and evaluate its properties *vis-a-vis* pure TiO₂. The deposition of CH₃NH₃PbI₃ on the mesoporous films was processed by spin-coating of a 30 wt% precursor solution, consisting of 1 : 1 mole ratio of CH₃NH₃I and PbI₂ in γ -butyrolactone (GBL). Annealing resulted in a change in the colour of the film from light yellow to dark brown, indicating the formation of CH₃NH₃PbI₃.⁴

Bright field (BF) TEM examination (Fig. 1a) of the 0.5%Y–TiO₂/CH₃NH₃PbI₃ electrode revealed the presence of aggregated TiO₂ nanoparticles deposited with ultrafine dark-contrast nanoparticles with a narrow size distribution of 5.8 ± 1 nm (Fig. 1e). High-resolution TEM (HRTEM) of aggregated particles (Fig. 1b) showed lattice fringes with a *d* spacing of 1.89 Å, corresponding to the (200) plane of tetragonal TiO₂ (JCPDS no. 21-1272). Similarly, HRTEM of ultrafine dark coloured individual nanoparticles (Fig. 1b) reveals lattice fringes with a *d* spacing of 7.2 Å that could be indexed to the (110) plane of the tetragonal phase of CH₃NH₃PbI₃,¹⁸ which is inter-related to the Fast Fourier Transform (FFT) pattern (Fig. 1c). The BFTEM image (Fig. 1f) of a pure TiO₂ sample showed the presence of irregularly shaped nanoparticles, supporting dark-contrast nanoparticles with a size distribution of 9.9 ± 0.9 nm (Fig. 1j). The HRTEM micrograph obtained from smaller nanoparticles (Fig. 1g) features lattice fringes with a *d* spacing of 7.2 Å that could be indexed to the (110) plane of the tetragonal phase of CH₃NH₃PbI₃, which is consistent with the FFT pattern (Fig. 1h).

The lattice fringes with a *d* spacing of 1.89 Å ((200) plane of tetragonal TiO₂), which could not be seen clearly in Fig. 1g, are shown in Fig. S1.†

Comparative analysis of BFTEM in combination with HRTEM and histograms reveals that the dimensions of perovskite nanoparticles supported on 0.5%Y–TiO₂ are smaller than those supported on pure TiO₂. Therefore, a higher loading of perovskite nanomaterial on the mesoporous 0.5%Y–TiO₂ film than on the mesoporous TiO₂ film is possible. It is to be noted that histograms, as shown in Fig. 1e and j, were constructed manually from the corresponding BFTEM micrographs.

Photovoltaic data

PV devices with different photoanodes were constructed in the same way. Their current–voltage (*J*–*V*) properties were measured under dark and AM 1.5G sun illumination (100 mW cm⁻²). Fig. 2 shows the *J*–*V* characteristics of the heterojunction solar cells

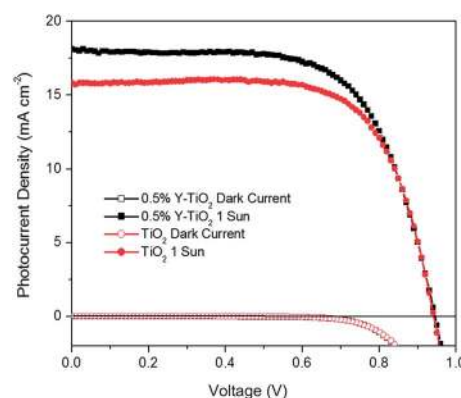


Fig. 2 Current–voltage characteristics of the heterojunction solar cells based on 0.5%Y–TiO₂ (black) and TiO₂ (red) measured under dark, and under 100 mW cm⁻² photon flux (1 sun).

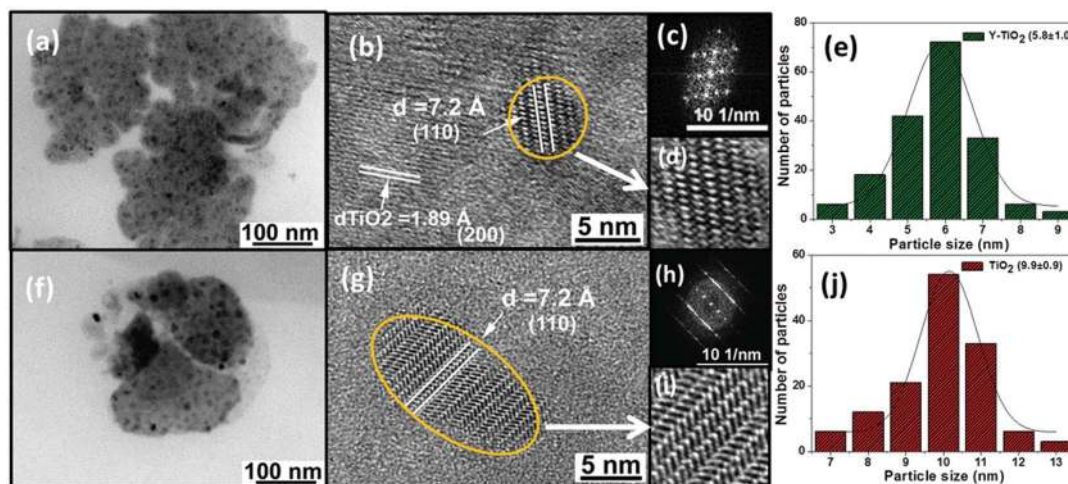


Fig. 1 TEM analysis of 0.5%Y–TiO₂/CH₃NH₃PbI₃ and TiO₂/CH₃NH₃PbI₃ electrodes: (a–e) 0.5%Y–TiO₂/CH₃NH₃PbI₃ electrode and (f–j) TiO₂/CH₃NH₃PbI₃ electrode: (a and f) BFTEM micrographs; (b and g) HRTEM micrographs of dark colored (encircled) individual nanoparticles deposited on TiO₂; (c and h) FFT patterns obtained from the corresponding HRTEM; (d and i) zoomed HRTEM showing prominent lattice fringes; (e and j) histograms showing particle size distribution.

based on the structure: FTO/10 nm compact TiO₂/mesoporous 0.5%Y-TiO₂ or TiO₂/CH₃NH₃PbI₃/spiro-OMeTAD/Au. The reference film displayed a short-circuit current density (J_{sc}), open-circuit voltage (V_{oc}) and fill factor (FF), respectively, of 15.8 mA cm⁻², 942 mV and 0.7, leading to a PCE of 10.5%. The device fabricated with the 0.5%Y-TiO₂ resulted in a higher J_{sc} of 18.1 mA cm⁻², yielding a PCE of 11.2% (Table 1). We attribute this considerable improvement to the difference in the growth of the perovskite on the mesoporous film.

In order to properly observe the change obtained across samples, 15 different solar cells were made under the same conditions for both 0.5%Y-TiO₂ and TiO₂. 53% of the cells with 0.5%Y-TiO₂ show a PCE of more than 11%, and the rest give a PCE between 10 and 11% (Fig. 3). In the case of TiO₂, 60% of the cells give a PCE between 10 and 11%, and the rest between 9 and 10% (Fig. S2[†]), pointing towards the good reproducibility of the system.

The incident photon-to-current conversion efficiency (IPCE) spectra show a current response from 400 to 800 nm, with a maximum of more than 75% in the wavelength range of 450–600 nm for 0.5%Y-TiO₂, and more than 65% for TiO₂ (Fig. 4). The inset (Fig. 4) shows the UV-vis absorbance spectra of photoanodes, *i.e.*, 0.5%Y-TiO₂/CH₃NH₃PbI₃ and TiO₂/CH₃NH₃PbI₃ films. Despite employing the same thickness of the mesoporous films and the same CH₃NH₃PbI₃ deposition method, the 0.5% Y-TiO₂ film exhibits higher absorbance than TiO₂ from the visible to the near IR region. This stronger absorbance indicates

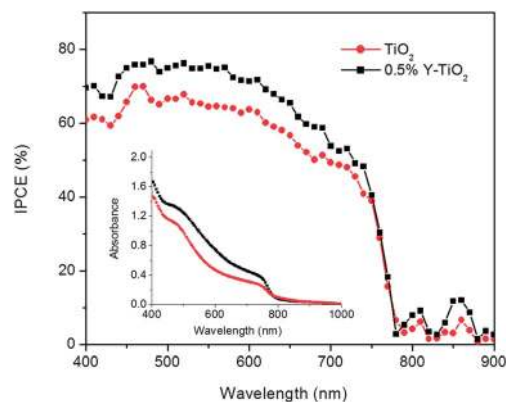


Fig. 4 The incident photon-to-electron conversion efficiency spectra of the devices based on 0.5%Y-TiO₂ (black) and TiO₂ (red). The inset shows the UV-vis absorbance spectra of 0.5%Y-TiO₂/CH₃NH₃PbI₃ and TiO₂/CH₃NH₃PbI₃ electrodes.

that more CH₃NH₃PbI₃ is supported by the 0.5%Y-TiO₂. Both 0.5%Y-TiO₂ and TiO₂ pastes have a similar particle size, pore size, and surface area. Thus the presence of merely 0.5%Y substitution not only shows a crucial effect on the crystal growth on the surface of the film, but also a significant improvement of perovskite absorber loading, which is consistent with the higher J_{sc} and IPCE. In keeping with this interpretation is the observation that the light harvesting efficiency (LHE) of cells employing the 0.5%Y-TiO₂ is substantially higher in the wavelength range between 500 and 800 nm than that for the unsubstituted TiO₂ particles. This is shown in Fig. S3 of the ESI.[†] However, below 500 nm the LHE of both types of films is similar and close to 100%. The fact that the IPCE remains higher for 0.5%Y-TiO₂ compared to TiO₂ indicates that, apart from the light harvesting, the quantum yields for carrier injection and/or recombination must be increased by Y substitution.

Kelvin probe force microscopy

In order to investigate the homogeneity of the electrical properties of the material in the devices we performed Kelvin probe force microscopy (KPFM). KPFM is able to detect local variations of the contact potential difference (CPD) in the range of several tens of nanometers.¹⁹ Illumination of samples with light allows the study of the photo-response of optoelectronic materials.^{20–22} In particular, it was reported that the measured shift in CPD upon illumination could be correlated with the HOMO and LUMO levels of the donor and acceptor materials.²³ In our setup, the illumination of the samples was provided from underneath (Fig. 5a). First, we recorded the topography of the hole-conducting layer spiro-OMeTAD (upper layer materials in our device) of the sample containing the pure TiO₂ (Fig. 5b, left) and compared that with the one recorded on the sample containing the 0.5%Y-TiO₂ (Fig. 5b, right). Both topographies showed a rather small rms roughness of 4 nm (TiO₂) and 7 nm (0.5%Y-TiO₂) for an area of 1 μm², respectively. Consecutively, we studied the electrical properties exemplarily for the pure TiO₂ sample at the identical position. The KPFM measurement in darkness (Fig. 5c, bottom) revealed a CPD between 0.33 and

Table 1 Photovoltaic parameters derived from J - V measurements for CH₃NH₃PbI₃-based devices on 0.5%Y-TiO₂ and TiO₂^a

	J_{sc} (mA cm ⁻²)	V_{oc} (mV)	FF	PCE (%)
0.5%Y-TiO ₂	18.1	945	0.66	11.2
TiO ₂	15.8	942	0.70	10.5

^a All devices were masked with an aperture area of 0.285 cm².

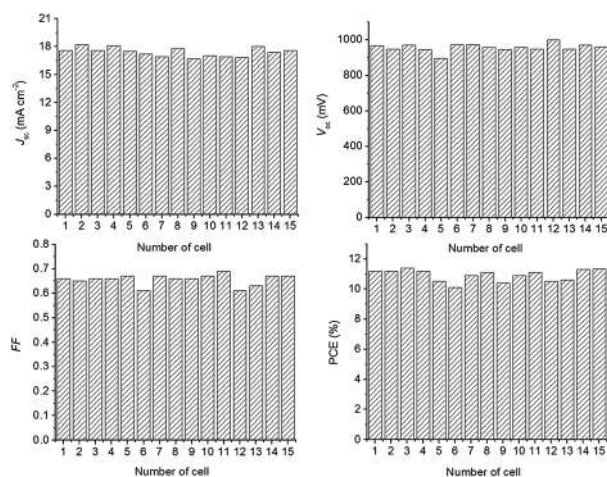


Fig. 3 Histogram plots of solar cell performance parameters for 15 cells: J_{sc} , V_{oc} , FF, and PCE for cells based on 0.5%Y-TiO₂.

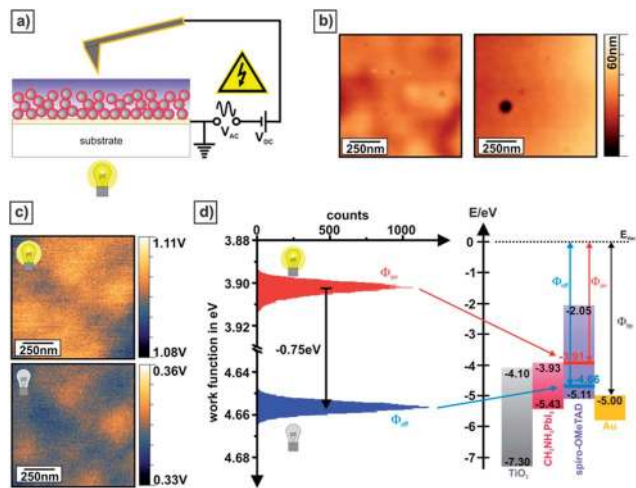


Fig. 5 Study of the photo-response on the hole-conducting layer of the devices by KPFM. (a) Schematic of the KPFM setup with integrated sample illumination from underneath the solar cell. (b) Topography images recorded on the pure TiO₂ sample (left) and on the 0.5%Y-TiO₂ sample (right). (c) CPD maps recorded on the pure TiO₂ sample on identical positions in darkness (bottom) and under illumination (top). (d) The corresponding work function distribution in darkness (blue peak) and under illumination (red peak) measured on one representative position of the sample. Upon illumination the work function decreased by around 0.75 eV. The resulting energy level $E_{\text{off}} = -4.66$ eV measured in darkness is slightly larger than the literature value of the HOMO level $E_{\text{HOMO}} = -5.11$ eV, which can be attributed to the high intensity of the super-luminescent diode ($\lambda = 860$ nm) that is used in the optical lever system of the scanning probe microscope. This intense illumination caused already a build-up of positive charge carriers in the spiro-OMeTAD layer that leads to an effective decrease of the work function of the spiro-OMeTAD.

0.36 V. Hence, both the roughness and CPD display a rather homogenous distribution. In a subsequent scan at the same position the CPD was recorded under illumination with $\lambda = 488$ nm (Fig. 5c, top). It was found that the measured CPD shifted by several hundred mV to values between 1.08 and 1.11 V. This shift was completely reversible after switching off the laser. Similar shifts upon illumination were confirmed for all measurements at different positions.

For a quantitative discussion of this photo-response, the CPDs measured in darkness (blue peak) and under illumination (red peak) were converted into work functions by taking into account the work function of the cantilever $\phi_{\text{tip}} = 5.00$ eV \pm 0.01 eV. These work functions were plotted *versus* the number of counts in a histogram (Fig. 5d, left). For each measurement we calculated the mean work function and its standard deviation. In darkness, the work function amounts to $\phi_{\text{off}} = 4.66$ eV \pm 0.01 eV. In terms of the energy level diagram, this work function corresponds to an energy level of $E_{\text{off}} = E_{\text{vac}} - \phi_{\text{off}} = -4.66$ eV as depicted schematically in the energy level diagram (Fig. 5d, right). Under illumination, the work function decreased by around 0.75 eV to $\phi_{\text{on}} = 3.91$ eV \pm 0.01 eV, resulting in an increased energy level of $E_{\text{on}} = E_{\text{vac}} - \phi_{\text{on}} = -3.91$ eV due to the accumulation of positive charge carriers in the spiro-OMeTAD layer upon light absorption. The energy E_{on} coincides well with the E_{LUMO} of CH₃NH₃PbI₃, which is correlated with the

equilibrium state between charge separation and recombination. In addition, this photo-response largely corresponds to the V_{oc} of the devices defined as the energy gap between the LUMO of the TiO₂ and the HOMO of the spiro-OMeTAD. The KPFM results are in good agreement with $V_{\text{oc}} = 0.9$ eV (Table 1) obtained for current-voltage bulk measurements at the same light intensity. This agreement confirms the efficiency of the process in these mesoscopic devices.

Impedance spectroscopy

Impedance spectroscopy (IS) was employed to investigate the influence of Y on the conduction band position of TiO₂ and/or the charge transfer processes. Minute changes can be observed in the dark current response (Fig. 6a, recorded during the IS measurements), showing a lower current for the 0.5%Y-TiO₂ devices.

Due to the absence of a full model to describe the device in an equivalent circuit several considerations have to be made in advance for the interpretation of the IS spectra and its results. The origin of an effect like a change in dark current observed with DSCs (dye sensitized solar cells) and ss-DSCs (solid state

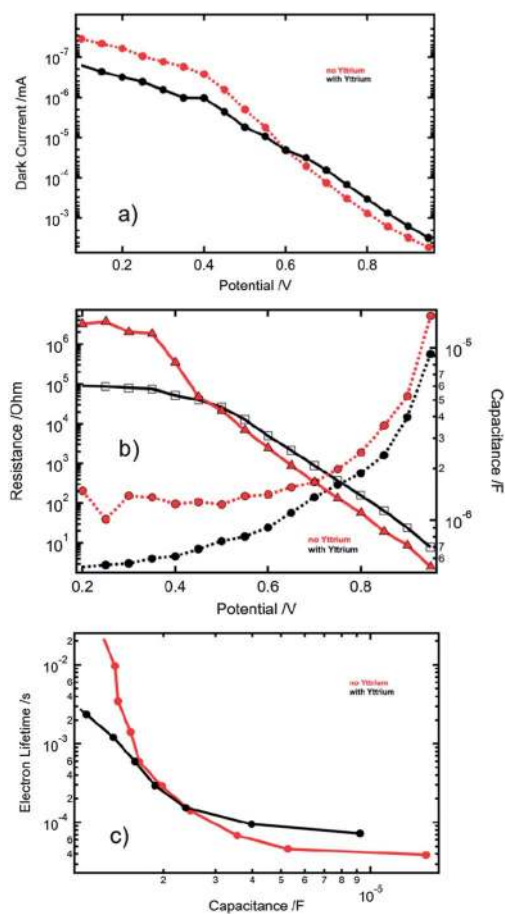


Fig. 6 Impedance spectroscopy results. (a) Dark current. (b) Recombination resistance (solid lines) and accompanying capacitance (dashed lines). (c) Evolution of the electron lifetime as a function of capacitance from IS measurements for the devices based on 0.5%Y-TiO₂ (black) and TiO₂ (red).

dye sensitized solar cells) is normally associated with a conduction band shift of the mesoporous TiO₂ and/or a change in recombination resistance at the mesoporous TiO₂/electrolyte or HTM (hole transport material) interface. In closely related structures such as ss-DSCs the recombination or charge transfer resistance is dominated by the recombination at the blocking layer/HTM interface (at low forward bias) or at the mesoporous TiO₂/HTM interface (at higher forward bias). Here, the high coverage of the blocking layer and mesoporous TiO₂ with perovskite can lead to a more complicated situation. As shown by Lee *et al.*,⁷ Etgar *et al.*,⁵ and Chung *et al.*,³ the perovskite can act as an electron or hole transport material. The mesoporous TiO₂ could therefore only act as a scaffold and may not be involved in the charge transport like in the case of the devices studied by Lee *et al.*⁷ employing an insulating mesoporous scaffold. The devices with CH₃NH₃PbI₃ on mesoporous Al₂O₃ show relatively low efficiency (about 4 to 5% PCE). This indicates that while the CH₃NH₃PbI₃ perovskite can transport electrons the mesoporous TiO₂ shows high efficiencies and is therefore electronically active. This is confirmed by the Nyquist plots showing the 45° transmission line at intermediate potentials (Fig. S4†) which can be attributed to the transport of charges across the nanocrystalline TiO₂ film. In contrast, with the perovskite deposited on mesoporous Al₂O₃, no such transmission line is observed, clearly indicating that the electrons are not flowing over the mesoporous Al₂O₃.

Kim *et al.* have shown that the recombination resistance dominating the current response of the devices can be identified and is, in the dark, related to the element appearing at lower frequencies.⁶ (It should be mentioned that sometimes a phenomenon called “negative” capacitance could be observed at even lower frequencies at high forward bias²⁴ representing presumably ionic movement). The capacitance associated with the recombination resistance is, in the low forward bias region when the mesoporous TiO₂ is still nonconductive, related to the space charge capacitance at the blocking layer.²⁵ At higher forward bias it represents the chemical capacitance of the mesoporous TiO₂, accounting for the occupation of the bulk trap states in the DOS by the injected electrons.²⁶ In depth investigations on the IS response of these types of devices are being conducted and will be published as soon as a reliable model for the whole system can be proposed.

Meanwhile we focus on the behavior of the mesoporous TiO₂ and fit its frequency response with a simple resistance and capacitance in parallel, the resistance representing the charge transfer resistance of the TiO₂ and the capacitor being the chemical capacitance as explained above. In the fitting procedure the capacitor for the chemical capacitance was replaced with a Constant Phase Element (CPE) accounting for *e.g.* the roughness and porosity of the TiO₂ (see also the experimental part). At low forward bias (<400 mV, Fig. 6b) where the current is channelled across the TiO₂ blocking layer/HTM interface the IS analysis shows a relatively constant resistance and capacitance. Upon increasing the forward bias the recombination resistance starts to decrease associated with an increase in dark current and the chemical capacitance starts to rise, representing the

increased filling of the DOS of the mesoporous TiO₂ layer. A small shift (~20 mV) of the capacitance of the sample with 0.5% Y-TiO₂ to higher forward potentials compared to the sample without Y can be observed. This indicates an upward shift of the conduction band in 0.5%Y-TiO₂. It should be mentioned that also a change of the doping of the HTM can lead to such an observable shift. In any case, the shift of the chemical capacitance is too small to present a major influence on the injection of excited electrons from the perovskite leading to the observed higher J_{sc} .

Apart from this shift, the capacitances showed a similar shape at higher forward bias indicating an equal distribution of the DOS as Chandiran *et al.*¹² have also observed. The shift of the recombination resistance is slightly larger, about 30 mV, which shows a slower recombination in the 0.5%Y-TiO₂. This can be clearly observed when plotting the electron lifetime ($\tau_n = R_{CT} \times C_{Chem}$) against the chemical capacitance (Fig. 6c). With such a representation any effects from the conduction band shift or a change of the doping level of the HTM are eliminated. One of the preconditions for this assumption is that the DOS has a similar distribution, which seems to be given in our case as visible by the shapes of the capacitance. The electron lifetimes show the same tendencies with slightly higher values for 0.5%Y-TiO₂ at higher forward bias though also here the effect is small.

On the basis of these impedance results it can be concluded that the presence of Y leads to a small increase of the electron lifetime and a minor conduction band move to higher energies. Both effects though cannot be the main reason for the observed increase in J_{sc} . Particularly the shift of the conduction band in the devices with Y-TiO₂ would lead to a reduced injection of electrons from the absorber.

Conclusion

We have demonstrated an enhanced PCE with the use of 0.5% Y³⁺ substitution of TiO₂ in the solid-state CH₃NH₃PbI₃-based mesoscopic solar cells. With the one-step spin-coating process, the devices using 0.5%Y-TiO₂ as the photoanode and spiro-OMeTAD as the hole transfer material yielded a PCE of 11.2% under 1 Sun illumination. A remarkable 15% increase in short circuit current density (2.3 mA cm⁻²) in the presence of Y is mainly attributed to its effect on surface modification. Yttrium is poorly soluble in TiO₂ and segregation of Y₂O₃ at the surface facilitates an increased material loading as shown by the increased light absorption of the deposited perovskite on TiO₂. Impedance spectroscopy confirms that neither the conduction band position nor the charge recombination process was influenced to a significant extent. Scanning probe microscopy allowed us to prove that the contact potential difference is homogeneously distributed at least on a 1 μm length scale. The localized properties complement the bulk properties, which clearly illustrates the efficient photo-induced charge separation process taking place in the cell. The surface substitution and/or the electronic structure modification of the semiconductor are effective ways for further improvement of the device performance in the mesoscopic cells.

Experimental details

Solar cell fabrication

CH₃NH₃I was synthesized as reported earlier.⁵ γ -Butyrolactone (GBL) and PbI₂ were ordered from Sigma-Aldrich. All the other chemicals were purchased from commercial sources and used without further purification. The precursor solution of perovskite was prepared by mixing the powder of CH₃NH₃I and PbI₂ at 1 : 1 mole ratio in GBL at 60 °C for 12 h, and used for the *in situ* formation of CH₃NH₃PbI₃.

The etched fluorine-doped tin oxide (FTO) conductive glass (TEC 7, Pilkington) was cleaned with 2% helmanex aqueous solution, acetone, and ethanol, successively. A 10 nm compact TiO₂ layer was deposited by atomic layer deposition (ALD, TDMAT, 150 °C).²⁷ The mesoporous film was prepared by spin-coating the TiO₂ or 0.5%Y-TiO₂ paste at 2000 rpm for 30 s, followed by sintering at 500 °C for 30 min in air. The prepared perovskite precursor solution was dropped on the semiconductor surface, and spin-coated at 1500 rpm for 30 s in the dry air box. The film was then annealed at 100 °C for 10 min.

The HTM, consisting of 0.06 M spiro-OMeTAD, 0.03 M lithium bis(trifluoromethylsulfonyl)imide (LiTFSI), 0.2 M 4-*tert*-butylpyridine (TBP), and 1% of tris(2-(1H-pyrazol-1-yl)-4-*tert*-butylpyridine)cobalt(III) tris(bis(trifluoromethylsulfonyl)imide) in chlorobenzene, was spin-coated on the top of the perovskite layer with the spin speed of 4000 rpm. Finally, 70 nm of Au was deposited by thermal evaporation at a pressure of 5×10^{-6} torr on the top of the HTM, as the counter electrode.

Photovoltaic characterization

The current–voltage characteristics were measured by applying an external potential bias to the device, and the generated photocurrent was recorded with a Keithley model 2400 digital source meter. A 450 W xenon lamp (Oriol) was used as the light source, equipped with a Schott K133 Tempax sunlight filter to reduce the mismatch between the simulated light and the AM 1.5G standard. IPCE spectra were measured with a 300 W xenon lamp (ILC technology). The light passed through a Genimi-180 double monochromator (Jobin Yvon Ltd) before it illuminated the device. The spectra were recorded with a Keithley 2400 source meter under a constant white light bias of around 5 mW cm⁻². Both were measured by using a mask with an area of 0.285 cm².

Transmission electron microscopy

The samples were examined by bright-field, high-resolution electron microscopy and selected area electron diffraction (SAED) on a JEM-2100F field emission transmission electron microscope operating at an accelerating voltage of 200 kV. After scratching the film, the powder obtained was dispersed in dichloromethane by sonication. Finally, the TEM specimen was prepared by slow evaporation of the diluted solution (40 μ L), and deposition on a formvar-coated copper grid.

Kelvin probe force microscopy

KPFM measurements were performed using a MFP-3D stand-alone setup (Asylum Research). To prevent any degradation of the sample during the KPFM measurements, the setup was placed in a glove box that was purged with dry nitrogen (humidity <0.1%, oxygen <0.01%). For simultaneous sample illumination during the KPFM measurement, the setup was equipped with a diode laser (Point Source, iFLEX2000) with a wavelength of 488 nm, an intensity of 13.3 mW on the sample, and a spot diameter of 640 μ m.²⁰ We used both sides of Cr/Au (5/25 nm)-coated cantilevers with a nominal vertical resonant frequency of 75 kHz (Olympus OMCL-AC240-TN). The KPFM measurements were performed in the dual pass mode at a lift height of 5 nm and with an AC voltage of 1.5 V. In KPFM, the contact potential difference (CPD) is measured which is defined as the difference in the work function between the tip and the sample. As we used the amplitude modulation mode of KPFM both the tip apex and the cantilever contribute to the measured CPD.²⁸ Thus, the magnitude of the measured local changes in CPD is reduced and does not fully correspond to the local difference in the work function between the tip and the sample. For the investigation of the work function shift upon sample illumination, we first calibrated the gold-coated cantilever on freshly cleaved, highly ordered pyrolytic graphite (HOPG). The measured CPD is defined by the following equation:

$$\text{CPD} = \frac{\Delta\Phi}{e} = \frac{(\Phi_{\text{tip}} - \Phi_{\text{sample}})}{e} \quad (1)$$

which is valid in the case where the AC potential is applied to the cantilever. Here, e is the elementary charge. HOPG has a work function of $\Phi_{\text{HOPG}} = 4.475 \pm 0.005$ eV.²⁹ The work function of the cantilever Φ_{tip} can then be calculated as:

$$\Phi_{\text{tip}} = e\text{CPD}_{\text{HOPG}} + \Phi_{\text{HOPG}} \quad (2)$$

with $e\text{CPD}_{\text{HOPG}} = 0.524 \pm 0.007$ eV. We determined the work function of the cantilever to be $\Phi_{\text{tip}} = 5.00 \pm 0.01$ eV.

Impedance spectroscopy

IS measurements were performed using a Biologic SP300 (Bio-Logic, France) in a frequency range between 7 MHz and 0.05 Hz for forward-bias potentials between 0 to 1 V (with a 10 mV sinusoidal AC perturbation) in 50 mV steps. The resulting impedance spectra were analyzed with the ZView software (Scribner Associate). The deviation from ideality in a CPE is expressed by the value n . With $n = 1$ the CPE is an ideal capacitor. Normally values between 0.8 and 1 are acceptable. n of the CPE used in the fitting procedure was not fixed and it was in the whole fitting range between 0.82 and 0.95.

Acknowledgements

The authors acknowledge financial contribution from Greatcell Solar SA, Epalinges, Switzerland, the King Abdullah University of Science and Technology (KAUST, Award no. KUS-C1-015-21), the European Community's Seventh Framework Programme

(FP7/2007–2013) under grant agreement no. 246124 of the SANS project, “ORION” grant agreement no. NMP-229036 and “CE-Mesolight” EPFL ECR advanced grant agreement no. 247404. MKN thanks the Global Research Laboratory (GRL) Program, Korea, and World Class University programs (Photovoltaic Materials, Department of Material Chemistry, Korea University) funded by the Ministry of Education, Science and Technology through the National Research Foundation of Korea (no. R31-2008-000-10035-0). ALD thanks the International Training Research Group 1404 (IRTG) “Self-Organized Materials for Optoelectronics” and the Deutsche Forschungsgemeinschaft (DFG) for their financial support. The authors thank Carole Grätzel, Shaik Mohammed Zakeeruddin and S. A. Shivashankar, IISC for helpful discussion.

References

- 1 M. Grätzel, *Acc. Chem. Res.*, 2009, **42**, 1788; S. Ahmad, E. G. Rodriguez, L. Kavan, M. Grätzel and M. K. Nazeeruddin, *Energy Environ. Sci.*, 2013, **6**, 3439.
- 2 A. Hagfeldt, G. Boschloo, L. Sun, L. Kloo and H. Pettersson, *Chem. Rev.*, 2010, **110**, 6595.
- 3 I. Chung, B. Lee, J. He, R. P. H. Chang and M. G. Kanatzidis, *Nature*, 2012, **485**, 486.
- 4 A. Kojima, K. Teshima, Y. Shirai and T. Miyasaka, *J. Am. Chem. Soc.*, 2009, **131**, 6050.
- 5 L. Etgar, P. Gao, Z. Xue, P. Qin, A. K. Chandiran, B. Liu, M. K. Nazeeruddin and M. Grätzel, *J. Am. Chem. Soc.*, 2012, **134**, 17396.
- 6 H.-S. Kim, C.-R. Lee, J.-H. Im, K.-B. Lee, T. Moehl, A. Marchioro, S.-J. Moon, R. Humphry-Baker, J.-H. Yum, J. E. Moser, M. Grätzel and N.-G. Park, *Sci. Rep.*, 2012, **2**, 591.
- 7 M. M. Lee, J. Teuscher, T. Miyasaka, T. N. Murakami and H. J. Snaith, *Science*, 2012, **338**, 643.
- 8 J.-H. Im, C.-R. Lee, J.-W. Lee, S.-W. Park and N.-G. Park, *Nanoscale*, 2011, **3**, 4088; J. H. Noh, S. H. Im, J. H. Heo, T. N. Mandal and S. I. Seok, *Nano Lett.*, 2013, **13**, 1764.
- 9 J. Burschka, N. Pellet, S.-J. Moon, R. H. Baker, P. Gao, M. K. Nazeeruddin and M. Grätzel, *Nature*, 2013, **499**, 316.
- 10 M. Liu, M. B. Johnston and H. J. Snaith, *Nature*, 2013, **501**, 395.
- 11 A. K. Chandiran, F. Sauvage, M. Casas-Cabanas, P. Comte, S. M. Zakeeruddin and M. Grätzel, *J. Phys. Chem. C*, 2010, **114**, 15849.
- 12 A. K. Chandiran, F. Sauvage, L. Etgar and M. Grätzel, *J. Phys. Chem. C*, 2011, **115**, 9232.
- 13 A. K. Chandiran, N. Tetreault, R. Humphry-Baker, F. Kessler, E. Baranoff, C. Yi, M. K. Nazeeruddin and M. Grätzel, *Nano Lett.*, 2012, **12**, 3941.
- 14 T. C. Li, M. S. Góes, F. Fabregat-Santiago, J. Bisquert, P. R. Bueno, C. Prasittichai, J. T. Hupp and T. J. Marks, *J. Phys. Chem. C*, 2009, **113**, 18385.
- 15 A. Kay and M. Grätzel, *Chem. Mater.*, 2002, **14**, 2930.
- 16 E. Palomares, J. N. Clifford, S. A. Haque, T. Lutz and J. R. Durrant, *J. Am. Chem. Soc.*, 2003, **125**, 475.
- 17 M. Nanu, J. Schoonman and A. Goossens, *Nano Lett.*, 2005, **5**, 1716.
- 18 J. Qiu, Y. Qiu, K. Yan, M. Zhong, C. Mu, H. Yan and S. Yang, *Nanoscale*, 2013, **5**, 3245.
- 19 U. Zerweck, C. Loppacher, T. Otto, S. Grafström and L. M. Eng, *Phys. Rev. B: Condens. Matter Mater. Phys.*, 2005, **71**, 125424.
- 20 R. Berger, A. L. Domanski and S. A. L. Weber, *Eur. Polym. J.*, 2013, **49**, 1907.
- 21 H. Hoppe, T. Glatzel, M. Niggemann, A. Hinsch, M. Ch. Lux-Steiner and N. S. Sariciftci, *Nano Lett.*, 2005, **5**, 269.
- 22 V. Palermo, G. Ridolfi, A. M. Talarico, L. Favaretto, G. Barbarella, N. Camaioni and P. Samori, *Adv. Funct. Mater.*, 2007, **17**, 472.
- 23 D. J. Ellison, J. Y. Kim, D. M. Stevens and C. D. Frisbie, *J. Am. Chem. Soc.*, 2011, **133**, 13802.
- 24 J. Bisquert, *Phys. Chem. Chem. Phys.*, 2011, **13**, 4679.
- 25 A. Dualeh, T. Moehl, M. K. Nazeeruddin and M. Grätzel, *ACS Nano*, 2013, **7**, 2292.
- 26 J. Bisquert, *Phys. Chem. Chem. Phys.*, 2003, **5**, 5360.
- 27 N. Tetreault, É. Arsenault, L.-P. Heiniger, N. Soheilnia, J. Brillet, T. Moehl, S. Zakeeruddin, G. A. Ozin and M. Grätzel, *Nano Lett.*, 2011, **11**, 4579.
- 28 S. V. Kalinin and D. A. Bonnell, *Phys. Rev. B: Condens. Matter Mater. Phys.*, 2001, **63**, 125411.
- 29 W. N. Hansen and G. J. Hansen, *Surf. Sci.*, 2001, **481**, 172.